

Simultaneous Inhibition of Vanadium Dissolution and Zinc Dendrites by Mineral-Derived Solid-State Electrolyte for High-Performance Zinc Metal Batteries

Chuancong Zhou⁺, Zeyou Wang⁺, Qing Nan, Huan Wen, Zhenming Xu, Jie Zhang, Zejun Zhao, Jing Li, Zhenyue Xing, Peng Rao, Zhenye Kang, Xiaodong Shi,^{*} and Xinlong Tian^{*}

Abstract: Designing solid electrolyte is deemed as an effective approach to suppress the side reaction of zinc anode and active material dissolution of cathodes in liquid electrolytes for zinc metal batteries (ZMBs). Herein, kaolin is comprehensively investigated as raw material to prepare solid electrolyte (KL–Zn) for ZMBs. As demonstrated, KL–Zn electrolyte is an excellent electronic insulator and zinc ionic conductor, which presents wide voltage window of 2.73 V, high ionic conductivity of 5.08 mS cm^{−1}, and high Zn²⁺ transference number of 0.79. For the Zn//Zn cells, superior cyclic stability lasting for 2200 h can be achieved at 0.2 mA cm^{−2}. For the Zn//NH₄V₄O₁₀ batteries, stable capacity of 245.8 mAh g^{−1} can be maintained at 0.2 A g^{−1} after 200 cycles along with high retention ratio of 81 %, manifesting KL–Zn electrolyte contributes to stabilize the crystal structure of NH₄V₄O₁₀ cathode. These satisfying performances can be attributed to the enlarged interlayer spacing, zinc (de)solvation-free mechanism and fast diffusion kinetics of KL–Zn electrolyte, availably guaranteeing uniform zinc deposition for zinc anode and reversible zinc (de)intercalation for NH₄V₄O₁₀ cathode. Additionally, this work also verifies the application possibility of KL–Zn electrolyte for Zn//MnO₂ batteries and Zn//I₂ batteries, suggesting the universality of mineral-based solid electrolyte.

1. Introduction

Zinc metal batteries (ZMBs) are booming electrochemical energy storage device with the intrinsic advantages of high safety, low cost and environmental friendliness.^[1,2] Among the numerous cathode materials, vanadium-based oxides have abundant species, flexible structure, high capacity, and good structure stability at high current densities, and are considered as the ideal cathodes for ZMBs.^[3–5] However, the practical application of vanadium-based cathodes is still restricted by the serious vanadium dissolution during cycling process at low current densities, resulting in the failure of crystal structure and the attenuation of specific capacity.^[6–8]

Vanadium dissolution in liquid electrolyte is a common phenomenon occurring at the interface of electrolyte and vanadium-based cathodes, which is strongly associated with the pH values of electrolytes, type of zinc salts, and the reactivity of H₂O molecules. Based on the experimental studies and theoretical calculations in the previous literatures,^[9–11] both the structural H₂O molecules in solvated Zn²⁺ ions and the free H₂O molecules in liquid electrolyte are significant inducement for the vanadium dissolution behavior of vanadium-based cathodes, which can strongly interact with unsaturated coordination vanadium elements, and dissolve out in the form of soluble vanadium-based compounds, such as VO²⁺, VO₂⁺ and VO₂(OH)₂[−].^[8,12–14] Therefore, the scientific approach for inhibiting vanadium dissolution can be summarized as follows: (1) Minimizing the content of free H₂O molecules in the electrolyte to avoid direct contact between free H₂O molecules and vanadium-based cathodes; (2) Regulating the solvation structure of Zn²⁺ ions to block the interaction between structural H₂O molecules and vanadium-based cathodes.^[15,16] Under the

[*] C. Zhou,⁺ Q. Nan, J. Zhang, Z. Zhao, J. Li, Z. Xing, P. Rao, Z. Kang, X. Shi, X. Tian
School of Marine Science and Engineering, State Key Laboratory of Marine Resource Utilization in South China Sea, Hainan University, Haikou 570228, China
E-mail: shixiaodong@hainanu.edu.cn
tianxl@hainanu.edu.cn

Z. Wang⁺
China State Key Laboratory of Fine Chemicals, Dalian University of Technology, Dalian 116023, China

H. Wen
Guangxi Key Laboratory of Electrochemical Energy Materials, School of Chemistry and Chemical Engineering, Guangxi University, Nanning 530004, China
Z. Xu
College of Materials Science and Technology, Nanjing University of Aeronautics and Astronautics, Nanjing 210016, China

[†] These authors contributed equally.

guidance of these ideas, “salt-in-water” electrolytes,^[17] eutectic electrolytes,^[18] inorganic colloidal electrolytes,^[19] and gel electrolytes,^[20–22] have been reported to be effective in inhibiting vanadium dissolution.^[23–25] However, these electrolytes will inevitably weaken the intrinsic advantages of aqueous batteries, including non-flammability, high ionic conductivity, non-toxicity, and low cost.^[26,27]

Recently, solid-state electrolytes derived from the raw materials of ZnPS_3 ,^[28] Zn^{2+} coordinated carboxylate celluloses,^[29] Zn^{2+} conducted plastic crystal,^[30] and UiO-66 ,^[31] have been demonstrated as effective strategy to kill two birds with one stone through synchronously inhibiting the active material dissolution of cathode and minimizing the interfacial side reactions of zinc metal anode.^[32] Unfortunately, the current preparation process is overly dependent on the addition of binders, such as polyvinylidene fluoride and polytetrafluoroethylene, to enhance the mechanical strength and maintain the robust structure, severely reducing the ionic conductivity and electrochemical performance of solid-state electrolytes. Additionally, the reported solid-state electrolytes always need to be soaked in Zn^{2+} -containing solution to improve the zinc ion conductivity, which makes the preparation process complicated. Thus, it is an urgent demand but challenging to design solid-state electrolytes with facile preparation process, low cost, high ionic conductivity and high performance, to meet the economic and practical requirements of ZMBs.^[33]

Herein, a common natural mineral of kaolin (KL) is optimized as the raw material to fabricate solid-state electrolyte (KL–Zn) owing to the intrinsic advantages of abundant reserves, low cost, layered structure, electronic insulator and zinc ionic conductor. As expected, KL–Zn electrolyte delivers wide voltage window of 2.73 V (vs. Zn^{2+}/Zn), high ionic conductivity of 5.08 mS cm^{-1} , and high Zn^{2+} transference number of 0.79, effectively endowing dendrite-free zinc anode for Zn/Zn symmetric cells, which can be ascribed to the reduced side reactions and uniform zinc deposition behavior on the surface of zinc metal. Meanwhile, the $\text{Zn}/\text{NH}_4\text{V}_4\text{O}_{10}$ batteries with KL–Zn as the electrolyte exhibit high reversible capacity of 259.2 mAh g^{-1} and high-capacity retention ratio of 83 % at 0.5 Ag^{-1} after 200 cycles, which can be attributed to the effective inhibition of vanadium dissolution and stable crystalline structure of $\text{NH}_4\text{V}_4\text{O}_{10}$ cathode. This work may provide references for the design of mineral-based solid-state electrolyte, and promote its practical application in zinc-based secondary batteries.

2. Results and Discussion

As schematically elaborated in Figure 1a, the optimizing KL–Zn electrolyte is fabricated by the initial zinc ion exchange treatment of KL powder in the ZnSO_4 solution, and the final cold pressing treatment of KL–Zn powder, which is convenient for scale production. Figure S1 presents the macroscopic shape, surface morphology and element distribution of KL–Zn electrolyte, implying its robust structure and element composition of Al, Si, O and Zn.

According to the XRD patterns of KL (Figure 1b) and KL–Zn powder (Figure S2a), the common phase component is well assigned to $2\text{SiO}_2 \cdot \text{Al}_2\text{O}_3 \cdot 2\text{H}_2\text{O}$ (PDF#10-0446, $\text{Al}_2[(\text{OH})_4/\text{Si}_2\text{O}_5]$), certifying the stable crystal structure of KL even after zinc ion exchange process. In details, the crystalline structure of $\text{Al}_2[(\text{OH})_4/\text{Si}_2\text{O}_5]$ has a typical layered feature and belongs to the monoclinic crystal system, which is composed by the ordered $[\text{SiO}_4]$ tetrahedrons and $[\text{AlO}_2(\text{OH})_4]$ octahedrons. The characteristic (002) and (004) diffraction peaks with the highest intensity are located at 12.37° and 24.85° , corresponding to the large interplanar spacing of 0.715 nm and 0.358 nm, respectively. Meanwhile, a new diffraction peak is detected around 20° in the XRD pattern of KL–Zn, and well matched with the crystalline phase of $\text{ZnSO}_4 \cdot \text{H}_2\text{O}$ (PDF#74-1331), demonstrating the presence of $\text{ZnSO}_4 \cdot \text{H}_2\text{O}$ in KL–Zn after the zinc ion exchange process. Additionally, Fourier transform infrared spectra (FTIR) and Raman spectra are also conducted to verify the surface groups in KL–Zn electrolyte with liquid electrolyte (2 M ZnSO_4) and KL electrolyte as the references. For the FTIR spectra (Figure 1c), KL–Zn electrolyte has similar stretching and formation vibrations with KL, which can be identified as the characteristic modes of KL, indicating the main frame structure of $\text{Al}_2[(\text{OH})_4/\text{Si}_2\text{O}_5]$ in KL–Zn. For the Raman spectra (Figures 1d, S2b), the two sharp characteristic peaks around $3600\text{--}3700 \text{ cm}^{-1}$ belong to KL material, and the mild characteristic peaks around 1020 and 3500 cm^{-1} can be respectively affirmed as the active groups of $\nu(\text{SO}_4^{2-})$ and $\nu(\text{HOH-OSO}_3^{2-})$,^[34] which is close to those of liquid electrolyte, further confirming the presence of $\text{ZnSO}_4 \cdot \text{H}_2\text{O}$ in KL–Zn.

Figure S2c compares the N_2 isothermal absorption/desorption curves of KL–Zn and KL powder, and the corresponding surface area of KL–Zn ($11.6 \text{ m}^2 \text{ g}^{-1}$) is slightly smaller than that of KL ($18.6 \text{ m}^2 \text{ g}^{-1}$), indicating the attendance of $\text{ZnSO}_4 \cdot \text{H}_2\text{O}$ clogs the pore and reduces the specific surface area of KL–Zn. Furthermore, the element compositions of KL and KL–Zn powder are disclosed by an inductively coupled plasma (ICP) spectrometer. As summarized in Figure 1e, except for zinc element, the Al and Si element content has no significant differences, testifying the introduction of Zn element in KL–Zn. To investigate the influences of $\text{ZnSO}_4 \cdot \text{H}_2\text{O}$ on the microstructure of KL–Zn, the transmission electron microscope (TEM), high-angle annular dark field (HAADF), elemental mapping distribution and high-resolution TEM images of KL–Zn and KL have been conducted. Consequently, the TEM (Figures 1f, S3a) and HAADF images (Figures 1g, S3b) show the two-dimensional sheet structure, while the elemental mapping images (Figure 1h) imply the presence of Zn element. Additionally, as for the HRTEM images of KL (Figure S3c) and KL–Zn (Figure S4), the clear lattice stripes in the high-crystallinity regions (marked with cycles) can be assigned to the (110) lattice plane, and the corresponding lattice spacing for KL–Zn and KL is 0.47 nm and 0.44 nm, respectively, demonstrating the enlarged lattice spacing of KL–Zn after the introduction of $\text{ZnSO}_4 \cdot \text{H}_2\text{O}$, which is beneficial to reduce the migration energy barrier and facilitate the bulk diffusion kinetic of Zn^{2+} ions.

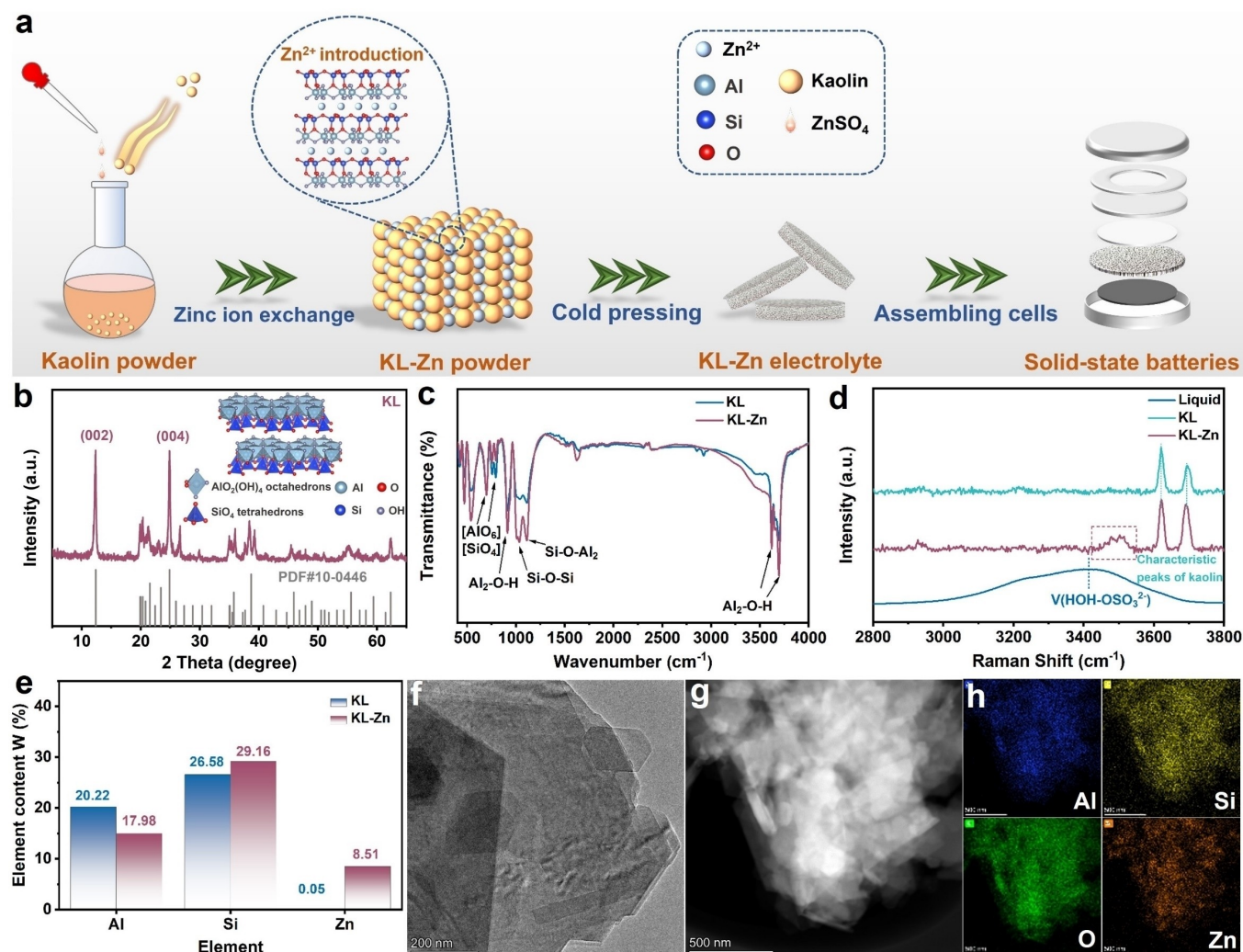


Figure 1. (a) Schematic diagram of the preparation process of KL-Zn electrolyte; (b) XRD pattern and crystalline structure of KL powder; (c) FTIR spectra and (d) Raman spectra of KL, KL-Zn, and liquid electrolytes; (e) Element content composition of KL and KL-Zn powder tested by ICP; (f) TEM image, (g) HAADF image, and (h) elemental mapping images of KL-Zn powder.

To evaluate the advantages of solid-state electrolyte in ZMBs, the electrochemical stable voltage window of KL-Zn and liquid electrolyte is measured by assembling Zn//Ti cells. As presented in Figure 2a, the stable voltage window for different electrolytes is 2.73 V and 2.11 V, respectively, while the broader voltage window of KL-Zn electrolyte suggests the effective inhibition of hydrogen evolution reaction and oxygen evolution reaction. Figure 2b exhibits the Tafel plots of Zn//Zn symmetric cells in different electrolytes, in which the lower corrosion current density (0.03 mA cm^{-2}) of KL-Zn means that solid-state electrolyte can greatly reduce the electrochemical corrosion of zinc metal induced by the interfacial side reactions. Figure 2c presents the current density-time curves of Zn//Zn symmetric cells in KL-Zn and liquid electrolytes tested by chronoamperometry (CA) method. Obviously, the CA curve in liquid electrolyte shows a sharp attenuation within the initial 25 s, and a continuous attenuation from 25 s to 300 s, which is a typical characteristics of two-dimensional

diffusion behavior of Zn^{2+} ions. In contrast, only a weak attenuation appears in the CA curve of KL-Zn electrolyte at first, and then remains stable, indicating an ordered three-dimensional diffusion behavior of Zn^{2+} ions in solid-state electrolyte.^[35,36] Figure 2d and Figure S5 deliver the current-time curves and the electrochemical impedances of Zn//Zn symmetric cells in KL-Zn and liquid electrolytes during the initial activation process, respectively. Based on the Equation S1 and Table S1, the calculated Zn^{2+} transference number in KL-Zn electrolyte is 0.79, which is twice as high as the value in liquid electrolyte (0.37), testifying the enhanced transfer capability of Zn^{2+} ions in KL-Zn electrolyte.

Additionally, the charge transfer resistances of Zn//Zn symmetric cells in KL-Zn and KL electrolyte (Figure S6) at different temperatures are also tested by electrochemical impedance spectroscopy (EIS) to calculate the corresponding activation energy barrier. According to the Equations S2, S3 and Table S2, the activation energy barrier of Zn//Zn

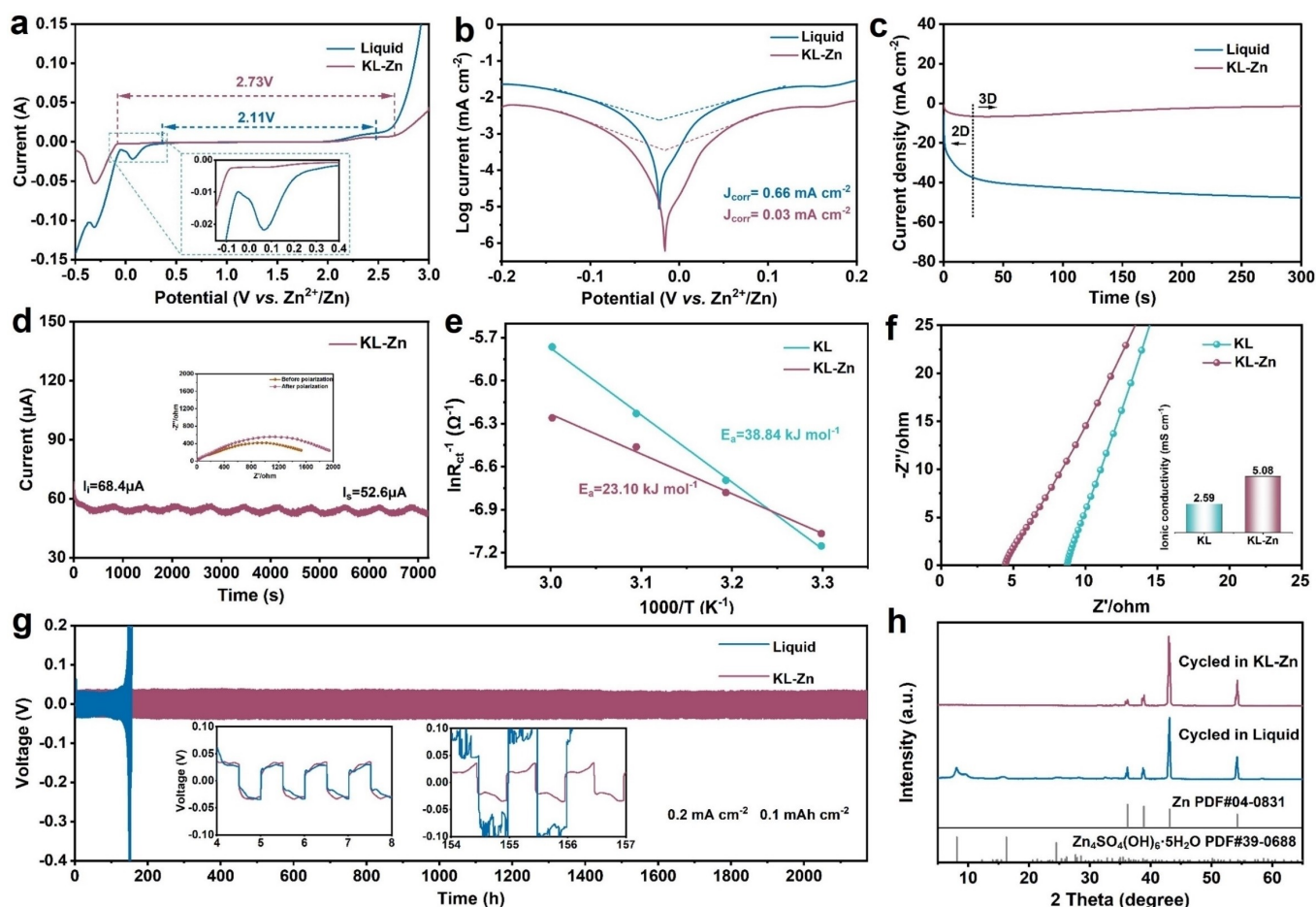


Figure 2. (a) Electrochemical stable voltage window of KL–Zn and liquid electrolytes; (b) Tafel and (c) Chronoamperometry curves of Zn//Zn symmetric cells in KL–Zn and liquid electrolytes; (d) Current-time curves and the Nyquist plots of Zn//Zn symmetric cells in KL–Zn electrolyte during the initial activation process; (e) The calculated activation energy barriers of Zn//Zn symmetric cells in KL–Zn and KL electrolytes; (f) Intrinsic impedances and the calculated ionic conductivity of KL and KL–Zn electrolytes; (g) Cycling performance of Zn//Zn symmetric cells in KL–Zn and liquid electrolytes under the test condition of 0.2 mA cm^{-2} – 0.1 mAh cm^{-2} ; (h) XRD patterns of zinc metal anode in Zn//Zn symmetric cells in KL–Zn and liquid electrolytes after 20 cycles.

symmetric cells in KL–Zn electrolyte (Figure 2e) is calculated to be 23.1 kJ mol^{-1} , much smaller than that in KL electrolyte ($38.84 \text{ kJ mol}^{-1}$), implying the fast interface reaction kinetics in KL–Zn electrolyte. The ionic conductivity of KL and KL–Zn electrolytes is calculated by assembling stainless-steel sheet cells and testing the intrinsic impedances. As presented in Figure 2f and Table S3, the ionic conductivity of KL–Zn is calculated to be 5.08 mS cm^{-1} , twice as high as the value of KL electrolyte (2.59 mS cm^{-1}), demonstrating that the introduced $\text{ZnSO}_4 \cdot \text{H}_2\text{O}$ in the ion exchange process plays a vital role in improving the ionic conductivity. Owing to the above-mentioned electrochemical advantages of KL–Zn electrolyte, the Zn//Zn symmetric cells in KL–Zn electrolyte can achieve an ultra-stable cycling performance for 2200 h at 0.2 mA cm^{-2} , while the corresponding cycle life in liquid electrolyte is only 154 h (Figure 2g). To uncover the causes for the performance differences, the XRD patterns and SEM images of zinc foil in Zn//Zn symmetric cells in different electrolytes after cycling are synchronously imple-

mented. Notably, the diffraction peaks belonging to the by-product of $\text{Zn}_4\text{SO}_4(\text{OH})_6 \cdot 5\text{H}_2\text{O}$ can be only detected on the surface of zinc foil in liquid electrolyte but not in KL–Zn electrolyte (Figure 2h), which is consistent with the intuitive result of SEM images (Figure S7), further demonstrating that solid-state electrolyte can greatly suppress the interfacial side reactions and the formation of by-products, so as to enhance the cycling reversibility and stability of Zn//Zn symmetric cells.^[37] As a direct verification, the electrochemical properties of the reported solid-state or quasi-solid-state electrolytes, such as Zn^{2+} transfer number, ionic conductivity, and cyclic life of Zn//Zn symmetric cells, have been summarized in Table S4, and the expected comparison results manifest the superiority of KL–Zn material as the solid-state electrolyte for ZMBs.

As proof of practical applications, the electrochemical performances of Zn// $\text{NH}_4\text{V}_4\text{O}_{10}$ batteries in both KL–Zn and liquid electrolytes are comprehensively investigated. XRD pattern of $\text{NH}_4\text{V}_4\text{O}_{10}$ material (Figure S8a) corresponds well with the standard card (PDF#31-0075), confirm-

ing the successful synthesis of $\text{NH}_4\text{V}_4\text{O}_{10}$. The SEM image of $\text{NH}_4\text{V}_4\text{O}_{10}$ material (Figure S8b) shows a flake morphology, and the layered crystal structure of $\text{NH}_4\text{V}_4\text{O}_{10}$ (Figure S8c) is conducive to the reversible (de)intercalation reaction of Zn^{2+} ions. Compared with liquid electrolyte, the normalized CV curves of $\text{NH}_4\text{V}_4\text{O}_{10}$ cathode in KL–Zn electrolyte (Figures 3a, S9) display similar redox peaks, larger enclosed areas, and higher consistency, revealing higher energy density and more stable redox reactions in solid-state electrolyte. Figure 3b represents the Nyquist plots of Zn// $\text{NH}_4\text{V}_4\text{O}_{10}$ batteries after CV tests in different electrolytes, and the smaller charge transfer resistance in KL–Zn electrolyte indicates the enhanced charge transfer behavior. Meanwhile, Figure S10 delivers the Nyquist plots of Zn// $\text{NH}_4\text{V}_4\text{O}_{10}$ batteries in KL–Zn electrolyte at different temperatures. Based on the Equations S2, S3 and Table S5, the activation energy barrier of Zn// $\text{NH}_4\text{V}_4\text{O}_{10}$ batteries in KL–Zn electrolyte is calculated as $23.86 \text{ kJ mol}^{-1}$, and the low activation energy barrier represents favorable reaction kinetics at the interface of $\text{NH}_4\text{V}_4\text{O}_{10}$ cathode and KL–Zn electrolyte. Figures 3c,d evaluate the self-discharge resistance capability of Zn// $\text{NH}_4\text{V}_4\text{O}_{10}$ batteries in KL–Zn and liquid electrolytes through 48 h shelving treatment after fully charged state. For the KL–Zn solid-state electrolyte, the voltage drop is about 0.23 V, and the reversible discharge capacity is $290.36 \text{ mAh g}^{-1}$ with high Coulombic efficiency

(CE) of 95.5 %. Even after three continuous self-discharge cycles, the reversible discharge capacity is $212.06 \text{ mAh g}^{-1}$ and the CE is still as high as 97.9 % (Figure S11a). In contrast, the corresponding voltage drop is 0.4 V in liquid electrolyte, and the discharge capacity is $207.15 \text{ mAh g}^{-1}$ with low CE of 66.5 %. After three continuous self-discharge cycles, the Zn// $\text{NH}_4\text{V}_4\text{O}_{10}$ batteries in liquid electrolyte only remain low capacity of $115.84 \text{ mAh g}^{-1}$ and low CE of 73.4 % (Figure S11b). This phenomenon can be ascribed to the inferior resistance to self-discharge behavior of Zn// $\text{NH}_4\text{V}_4\text{O}_{10}$ batteries in liquid electrolyte caused by the complex solid–liquid interface side reactions during the shelving process.

To further demonstrate the positive effects of solid-state electrolyte on inhibiting the vanadium dissolution of $\text{NH}_4\text{V}_4\text{O}_{10}$ cathode during cycling process, the cyclic performances of Zn// $\text{NH}_4\text{V}_4\text{O}_{10}$ batteries at low current densities have been contrasted. In details, the $\text{NH}_4\text{V}_4\text{O}_{10}$ cathode keeps high specific capacity of 245.8 mAh g^{-1} and high retention ratio of 81 % at 0.2 A g^{-1} after 200 cycles in KL–Zn electrolyte (Figure 3e), while the remaining capacity and retention ratio in liquid electrolyte is as low as 109.8 mAh g^{-1} and 34 % due to the unstable crystal structure of $\text{NH}_4\text{V}_4\text{O}_{10}$ cathode induced by the serious vanadium dissolution under low current densities. Similarly, the reversible capacity of $\text{NH}_4\text{V}_4\text{O}_{10}$ cathode in KL–Zn and

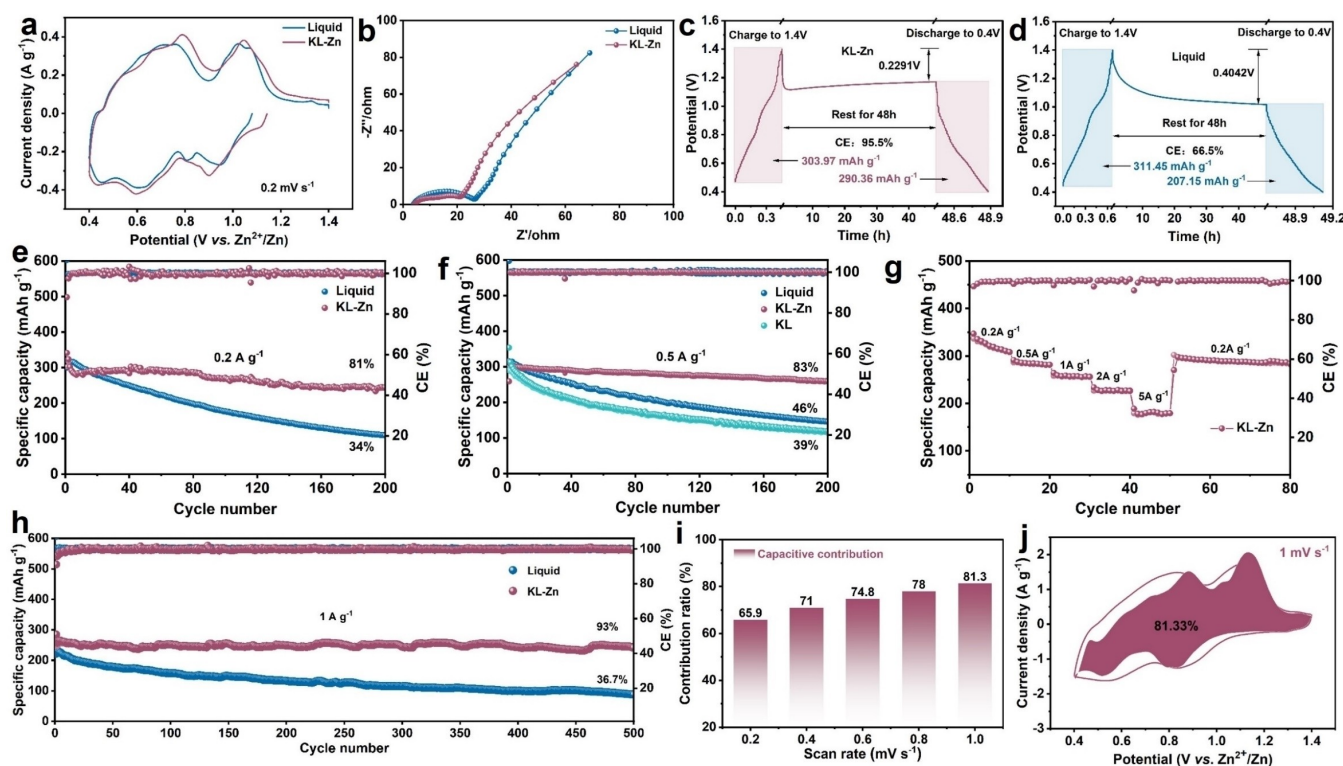


Figure 3. (a) Initial CV curves and (b) Nyquist plots of Zn// $\text{NH}_4\text{V}_4\text{O}_{10}$ batteries in KL–Zn and liquid electrolytes; Self-discharge resistance capability test of Zn// $\text{NH}_4\text{V}_4\text{O}_{10}$ batteries in (c) KL–Zn and (d) liquid electrolytes; Cycling performances of Zn// $\text{NH}_4\text{V}_4\text{O}_{10}$ batteries in KL–Zn and liquid electrolytes at the current density of (e) 0.2 A g^{-1} and (f) 0.5 A g^{-1} ; (g) Rate capability of Zn// $\text{NH}_4\text{V}_4\text{O}_{10}$ batteries in KL–Zn electrolyte at the current densities of 0.2, 0.5, 1, 2, and 5 A g^{-1} ; (h) Long-term cycling performances of Zn// $\text{NH}_4\text{V}_4\text{O}_{10}$ batteries in KL–Zn and liquid electrolytes at 1 A g^{-1} ; (i) The calculated capacitive contribution ratio of Zn// $\text{NH}_4\text{V}_4\text{O}_{10}$ batteries in KL–Zn electrolyte at the scan rate of 0.2–1.0 mV s^{-1} ; (j) Capacitive contribution area of Zn// $\text{NH}_4\text{V}_4\text{O}_{10}$ batteries in KL–Zn electrolyte at the scan rate of 1.0 mV s^{-1} .

liquid electrolytes are 259.2 and 146.7 mAhg⁻¹ at 0.5 Ag⁻¹ after 200 cycles in sequence (Figures 3f, S12), and their corresponding capacity retention ratio are 83 % and 46 %, respectively, further verifying solid-state electrolyte can improve the cycling stability of NH₄V₄O₁₀ cathode through effectively suppressing the vanadium dissolution. As a contrast sample, the specific capacity of NH₄V₄O₁₀ cathode in KL electrolyte sharply decreases from 290.6 to 114.7 mAhg⁻¹ at 0.5 Ag⁻¹ within 200 cycles, which can be attributed to its low ionic conductivity and poor vanadium dissolution inhibition ability. Additionally, the cycling stability of Zn//NH₄V₄O₁₀ batteries at low and high temperature conditions in different electrolytes also have been investigated. As exhibited in Figures S13, the corresponding specific capacity and capacity retention ratio of NH₄V₄O₁₀ cathode in KL–Zn electrolyte are far higher than those in liquid electrolyte, manifesting the wide operating temperature range of solid-state electrolyte for ZMBs.^[38] Furthermore, the cyclic stability of vanadium-based cathodes in different electrolytes at low current densities have been summarized in Table S6.^[39–49] After careful comparison, the high reversible capacity and high retention ratio of NH₄V₄O₁₀ cathode in KL–Zn electrolyte in this work verify the effective inhibition of vanadium dissolution to stabilize the crystal structure during cycling process.

Figure 3g displays the rate capability of NH₄V₄O₁₀ cathode in KL–Zn electrolyte, and the reversible capacity is 300, 284.6, 257.6, 225.9 and 182.2 mAhg⁻¹ at 0.2, 0.5, 1, 2, and 5 Ag⁻¹, respectively. After the current density recovering to 0.2 Ag⁻¹, the corresponding capacity can be raised to 288.4 mAhg⁻¹ and remains unchanged, suggesting the superior rate performance of NH₄V₄O₁₀ cathode in KL–Zn electrolyte. Figure 3h compares the long-term cycling performances of NH₄V₄O₁₀ cathode in different electrolytes at 1 Ag⁻¹. Briefly, the remained capacity of NH₄V₄O₁₀ cathode in KL–Zn and liquid electrolytes are 241.6 and 87.8 mAhg⁻¹ at 1 Ag⁻¹ after 500 cycles, corresponding to the capacity retention ratio of 93 % and 36.7 %, respectively, further confirming the stable crystal structure and suppressed vanadium dissolution of NH₄V₄O₁₀ cathode in solid-state electrolyte. Additionally, the NH₄V₄O₁₀ cathode in KL–Zn electrolyte also can maintain high reversible capacity of 195.9 mAhg⁻¹ after 1000 cycles at 4 Ag⁻¹ (Figure S14a), and 177.7 mAhg⁻¹ after 2600 cycles at 6 Ag⁻¹ (Figure S14b) without significant capacity attenuation, manifesting the superior structural stability and wide operating current range of both NH₄V₄O₁₀ cathode and KL–Zn electrolyte. Furthermore, the CV curves of Zn//NH₄V₄O₁₀ batteries at different scan rates (0.2–1.0 mVs⁻¹) and the *b* values corresponding to the redox peaks were tested to analyze the zinc storage behavior of NH₄V₄O₁₀ cathode in KL–Zn electrolyte. Notably, two couples of redox peaks can be observed (Figure S15a), implying the stepwise (de)intercalation reaction of Zn²⁺ ions in the crystal structure of NH₄V₄O₁₀. Based on the Equations S4, S5, the calculated *b* values for the four peaks (Figure S15b) are 0.808, 0.898, and 0.897 and 0.874, respectively, revealing that the zinc storage behavior of Zn//NH₄V₄O₁₀ batteries in KL–Zn electrolyte can be recognized as pseudocapacitive

adsorption reaction. Additionally, the pseudocapacitive contribution ratios at different scan rates can be quantitatively calculated based on the Equations S6, S7. As shown in Figures 3i,j, the pseudocapacitive contribution ratios are 65.9 %, 71 %, 74.8 %, 78 %, and 81.3 % at the scan rates of 0.2, 0.4, 0.6, 0.8, and 1.0 mVs⁻¹, respectively, suggesting the high pseudocapacitive contribution ratio at high scan rate.^[50]

In order to provenly confirm the inhibition of vanadium dissolution by solid-state electrolyte, the surface phases, surface groups, element compositions, element valence states, and micro morphology of NH₄V₄O₁₀ cathode, KL–Zn electrolyte and zinc metal anode have been systematically investigated by a series of material characterization techniques. As a result, the XRD patterns of NH₄V₄O₁₀ cathode at fully charged and discharged states (Figure S16) reveal that the by-products of Zn₃(OH)₂V₂O₇·2H₂O (PDF#50-0570) is only detected in liquid electrolyte, which is the main vanadium dissolution of vanadium-based cathodes. By analyzing the molecular formula of Zn₃(OH)₂V₂O₇·2H₂O, it is concluded the active H₂O molecules is a necessary condition to induce the formation of by-products, and solid-state electrolyte can realize free by-products by minimizing the content of active H₂O molecules and side reactions between vanadium-based cathodes and liquid electrolyte. These by-products will continue to accumulate on the surface of NH₄V₄O₁₀ cathode and consume liquid electrolyte as well as active vanadium during cycling process (Figures S17), so as to affect the cycling stability of Zn//NH₄V₄O₁₀ batteries.^[51,52] Subsequently, in situ Raman spectra of Zn//NH₄V₄O₁₀ batteries have been tested in both KL–Zn and liquid electrolytes to identify the crystal structure evolution of NH₄V₄O₁₀ cathode during the initial (dis)charge process. In details, the red signal areas around 150, 260/400, and 500 cm⁻¹ can be respectively assigned to the bending vibrations of δ(–O–V–O–V–) and δ(V=O), as well as the stretching vibration of ν(V–O).^[53] The regular signal changes in KL–Zn electrolyte (Figure 4a) demonstrate the reversible crystalline structure of NH₄V₄O₁₀ cathode during cycling, further testifying the effective vanadium dissolution inhibition of solid-state electrolyte. As a comparison, the Raman signals of NH₄V₄O₁₀ cathode in liquid electrolyte (Figure 4b) is untraceable, which may be attributed to the irreversible destruction of crystal structure induced by the severe vanadium dissolution.

The stable coordination environment of vanadium element in KL–Zn electrolyte can be proved by the high-resolution V 2p spectra of NH₄V₄O₁₀ cathode at different voltage states (Figures 4c, S18a). Notably, the pristine V 2p spectra is composed by the chemical valence states of V⁵⁺ and V⁴⁺, and the V³⁺ region appears at fully discharged state with the shrink of V⁵⁺ and V⁴⁺ regions due to the intercalation of Zn²⁺ ions. After returning to fully charged state, the V³⁺ region disappears with the deintercalation of Zn²⁺ ions (Figure 4d), and the corresponding regions of V⁵⁺ and V⁴⁺ can almost recover to the initial state, further demonstrating the reversible and stable crystal structure of NH₄V₄O₁₀ in KL–Zn electrolyte (Figures S19). Moreover, judging from the region changes of V⁵⁺ and V⁴⁺, the high-resolution V 2p spectra of NH₄V₄O₁₀ cathode after 20 cycles

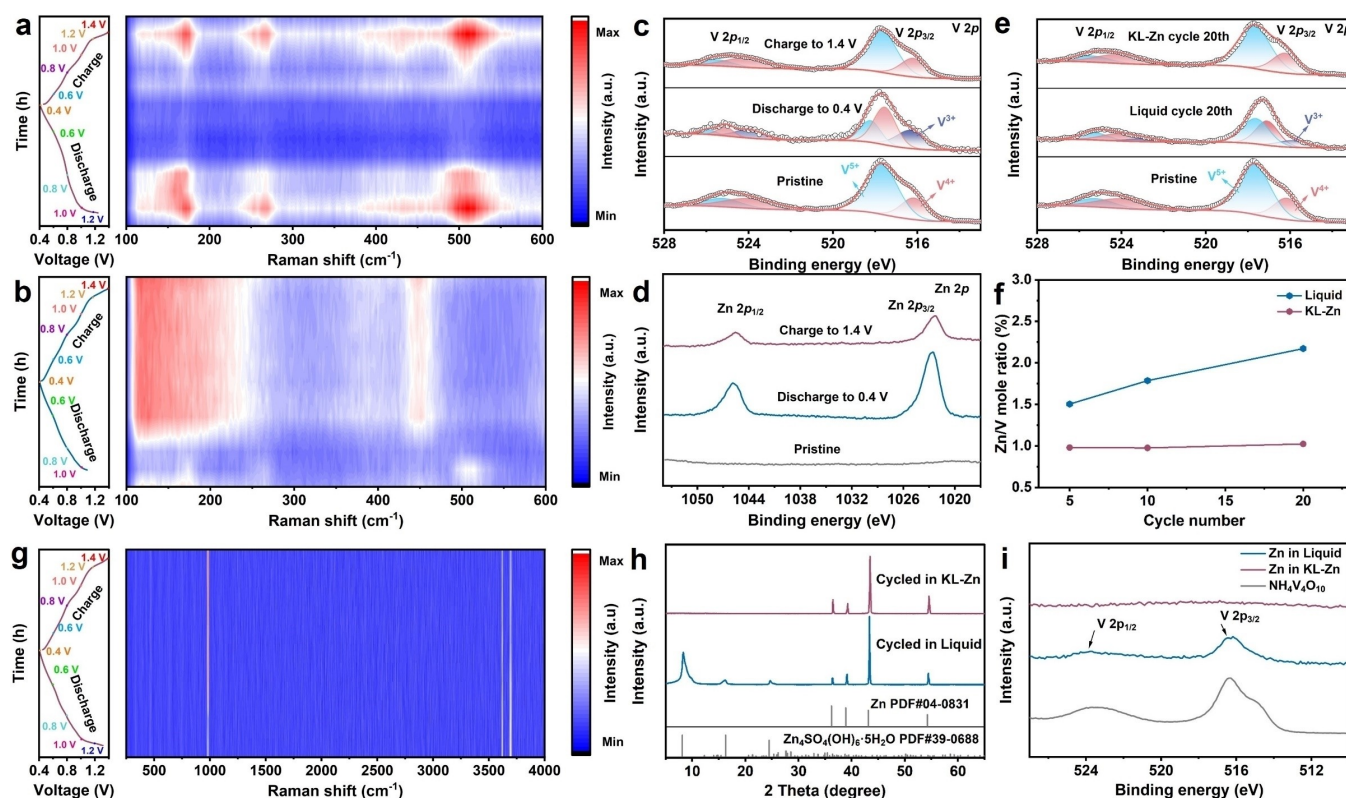


Figure 4. In situ Raman spectra of $\text{NH}_4\text{V}_4\text{O}_{10}$ cathode in (a) KL-Zn and (b) liquid electrolytes during cycling process; High-resolution (c) V 2p and (d) Zn 2p spectra of $\text{NH}_4\text{V}_4\text{O}_{10}$ cathodes at the pristine, fully discharged and fully charged states in KL-Zn electrolyte; (e) High-resolution V 2p spectra of $\text{NH}_4\text{V}_4\text{O}_{10}$ cathodes in KL-Zn and liquid electrolytes after 20 cycles; (f) Zn/V element content ratios of $\text{NH}_4\text{V}_4\text{O}_{10}$ cathodes after 5, 10, 20 cycles in KL-Zn and liquid electrolytes; (g) In situ Raman spectra of KL-Zn electrolyte during cycling process; (h) XRD patterns of zinc metal anode after 20 cycles in KL-Zn and liquid electrolytes; (i) High-resolution V 2p spectra of zinc metal anode in KL-Zn and liquid electrolytes after 20 cycles.

(Figures 4e, S18b) also verify the absent and severe vanadium dissolution in KL-Zn and liquid electrolytes, respectively. Additionally, as an ironclad proof for vanadium dissolution, the Zn/V content ratio of $\text{NH}_4\text{V}_4\text{O}_{10}$ cathode recorded by ICP remains nearly constant in KL-Zn electrolyte after 5/10/20 cycles, but gradually increases with the increase of cycle number in liquid electrolyte due to the continuous loss of vanadium content (Figure 4f).^[54] Figure 4g presents the in situ Raman spectra of KL-Zn electrolyte in $\text{Zn}/\text{NH}_4\text{V}_4\text{O}_{10}$ batteries to verify its structural stability during cycling process. Interestingly, the three Raman signals persisting around 1000 and 3600 cm^{-1} are respectively matched with the stretching vibration of $\nu(\text{SO}_4^{2-})$ and characteristic peaks of KL material, indicating the stable chemical property and crystal structure of KL-Zn electrolyte, which also can be confirmed by the XRD patterns of KL-Zn electrolyte in $\text{Zn}/\text{NH}_4\text{V}_4\text{O}_{10}$ batteries after different cycles (Figure S20).

Furthermore, the vanadium dissolution and shuttle effect in liquid electrolyte also have been uncovered by the XRD patterns, SEM images and XPS spectra of zinc foil in $\text{Zn}/\text{NH}_4\text{V}_4\text{O}_{10}$ batteries. As demonstrated, the by-products of $\text{Zn}_4\text{SO}_4(\text{OH})_6 \cdot x\text{H}_2\text{O}$ are observed on zinc foil in liquid electrolyte (Figure 4h), while the zinc foil in KL-Zn electrolyte has a flat, clean surface and almost no by-products

(Figure S21). Additionally, the survey XPS spectra (Figure S22), high-resolution V2p (Figure 4i) and S2p spectra (Figure S23) of zinc foil further confirms the existence of vanadium- and sulfur-containing by-products, suggesting the dissolved vanadium can pass through the separators in liquid electrolyte and precipitate on the surface of zinc foil.

To deeply recognize the unique characteristics and action mechanism of KL-Zn electrolyte, both the experimental measurement and DFT calculations have been performed. Figures 5a–c respectively present the energy band structure, density of states (DOS), and electron conductivity of KL-Zn electrolyte, and its band gap is as wide as 3.5 eV and its maximum electron conductivity is only about 0.6 $\mu\text{S cm}^{-1}$, verifying the electronic insulator property of KL-Zn electrolyte.^[55] The ionic conductivities of KL-Zn electrolyte within 30–60 °C (Figures S24) are also measured by firmly sandwiching between two stainless-steel plates, and the ionic conductivities are ranging from 5.08 to 10.48 mS cm^{-1} , higher than those of other quasi-solid-state electrolytes for ZMBs. Based on the Arrhenius formula and Table S7, the corresponding ionic migration energy barrier in KL-Zn electrolyte (Figure 5d) can be calculated as 21.2 kJ mol^{-1} , very close to the activation energy barrier of Zn/Zn symmetric cells in KL-Zn electrolyte (Figure 2e, 23.1 kJ mol^{-1}), which takes the total energy barrier of mass

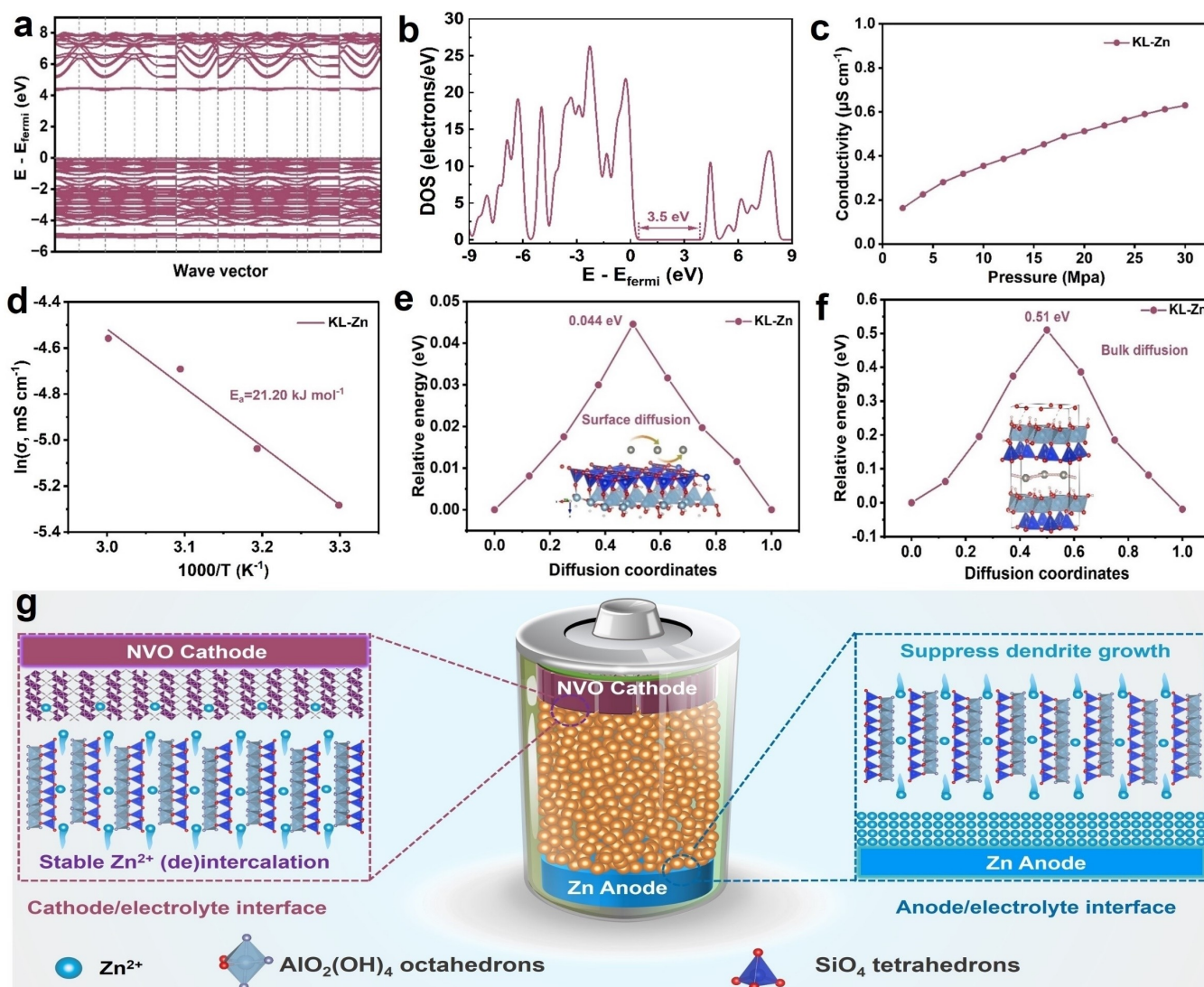


Figure 5. (a) Energy band structure, (b) density of state (DOS), and (c) electronic conductivity of KL–Zn electrolyte; (d) Ionic migration energy barrier, (e) surface diffusion energy barrier, and (f) bulk diffusion energy barrier for Zn^{2+} ions in the crystalline structure KL–Zn electrolyte; (g) Schematic illustration of the dual action mechanism of KL–Zn electrolyte for both zinc metal anode and $\text{NH}_4\text{V}_4\text{O}_{10}$ cathode of ZMBs.

and charge transfer processes into considerations. Additionally, the negligible energy barrier difference ($\Delta = 1.9 \text{ kJ mol}^{-1}$) means the (de)solvation-free process of Zn^{2+} ions in KL–Zn electrolyte.^[28,56] Figures 5e,f delivers the surface and bulk diffusion energy barriers, as well as the corresponding diffusion path of Zn^{2+} ions. As calculated, the surface and bulk diffusion energy barriers are as low as 0.044 and 0.51 eV, respectively, demonstrating its fast diffusion kinetic along with the interlayers, which can be mainly attributed to the intrinsic larger lattice spacing of KL–Zn. These results manifest that KL–Zn is an ideal solid-state electrolyte for Zn/ $\text{NH}_4\text{V}_4\text{O}_{10}$ batteries, which can act as the roles of both separator and electrolyte to block electron transport, promote zinc ion diffusion, and inhibit the vanadium dissolution. Figure 5g schematically illustrates the positive effects of KL–Zn electrolyte for both zinc metal anode and $\text{NH}_4\text{V}_4\text{O}_{10}$ cathode. For the anode/electrolyte interface, the unique layered structure of KL–Zn can

effectively endow Zn^{2+} ions fast diffusion kinetics, provide an order zinc ion transport channel, and guide a highly reversible plating/stripping behavior as well as dendrite-free zinc anode. For the cathode/electrolyte interface, the intrinsic solid-state and Zn^{2+} ions superconductor properties of KL–Zn electrolyte can availably inhibit the vanadium dissolution, avoid the interfacial side reactions, stabilize the lattice structure of $\text{NH}_4\text{V}_4\text{O}_{10}$ cathode and ensure a reversible (de)intercalation process of Zn^{2+} ions. In order to further verify the compatibility and practicality of KL–Zn electrolyte in other zinc-based batteries, $\alpha\text{-MnO}_2$ (Figures S25a,b) and UPC@I_2 material (Figures S25c,d) were successfully prepared according to the previous reports,^[57–59] and the galvanostatic cycling performance of Zn/ $\alpha\text{-MnO}_2$ batteries (Figures S26a,b) and Zn/ I_2 batteries (Figures S26c,d) in KL–Zn electrolyte were measured. In brief, the reversible capacity of $\alpha\text{-MnO}_2$ cathode in KL–Zn electrolyte maintains 236.4 mAh g^{-1} at 0.2 A g^{-1} , higher than that in

liquid electrolyte (155.8 mAhg^{-1}). For the Zn/I_2 batteries, the UPC@I_2 cathode delivers a high reversible capacity of 149.8 mAhg^{-1} after 160 cycles at 1 Ag^{-1} , manifesting the universality of KL-Zn electrolyte for vanadium-, manganese-, and iodine-based cathodes of ZMBs.

3. Conclusion

In summary, KL-Zn electrolyte is prepared for high-performance ZMBs with kaolin as the raw material. Benefiting from the anhydrous characteristic, KL-Zn electrolyte can deliver wide operating voltage window (2.73 V), high ionic conductivity (5.08 mS cm^{-1}), and high Zn^{2+} transference number (0.79). For the solid-state Zn/Zn cells, long-term cyclic stability for 2200 h can be achieved at the test condition of 0.2 mA cm^{-2} – 0.1 mAh cm^{-2} . For the solid-state $\text{Zn}/\text{NH}_4\text{V}_4\text{O}_{10}$ batteries, high reversible capacity of 241.6 mAhg^{-1} can be remained at high current density of 1 Ag^{-1} after 500 cycles along with high-capacity retention ratio of 93 %, manifesting superior structural stability of $\text{NH}_4\text{V}_4\text{O}_{10}$ cathode in solid-state electrolyte. Combined with the theoretical calculations, these interesting results can be mainly attributed to the two-dimensional layered structure, enlarged lattice spacing and low zinc diffusion barrier of KL-Zn material, which not only guides ordered zinc transport and reversible zinc deposition behavior at the interface of zinc anode, but also inhibits the vanadium dissolution and structural distortion at the interface of $\text{NH}_4\text{V}_4\text{O}_{10}$ cathode. This study will drive the design and application of mineral-based solid-state electrolytes, and promotes the development of durable aqueous secondary batteries.

Supporting Information

Supporting Information is available from the authors.

Acknowledgements

The authors thank the National Natural Science Foundation of China (52274297 and 52164028), Research Fund of the Innovation Platform for Academicians of Hainan Province (YSPTZX202315), Collaborative Innovation Center of Marine Science and Technology of Hainan University (XTCX2022HYC14), and Start-up Research Foundation of Hainan University (KYQD(ZR)-23069, 23169 and 20008). Additionally, the authors acknowledge the support for comprehensive characterizations by Pico Election Microscopy Center of Hainan University, and this work is partially supported by High Performance Computing Platform of Nanjing University of Aeronautics and Astronautics.

Conflict of Interest

The authors declare no competing interests.

Data Availability Statement

The data that support the findings of this study are available within the manuscript and the corresponding Supporting Information file.

Keywords: Kaolin • Solid-state electrolyte • Dendrite-free zinc anode • Inhibition of vanadium dissolution • Zinc metal batteries

- [1] S. W. Gourley, R. Brown, B. D. Adams, D. Higgins, *Joule* **2023**, 7(7), 1415–1436.
- [2] L. Wang, B. Zhang, W. Zhou, Z. Zhao, X. Liu, R. Zhao, Z. Sun, H. Li, X. Wang, T. Zhang, et al., *J. Am. Chem. Soc.* **2024**, 146(9), 6199–6208.
- [3] G. Li, L. Sun, S. Zhang, C. Zhang, H. Jin, K. Davey, G. Liang, S. Liu, J. Mao, Z. Guo, *Adv. Funct. Mater.* **2023**, 34(5), 2301291.
- [4] S. Liu, R. Zhang, C. Wang, J. Mao, D. Chao, C. Zhang, S. Zhang, Z. Guo, *Angew. Chem. Int. Ed.* **2024**, 63(17), e202400045.
- [5] Y. Liu, C. Lu, Y. Yang, W. Chen, F. Ye, H. Dong, Y. Wu, R. Ma, L. Hu, *Adv. Mater.* **2024**, 36(18), 2312982.
- [6] Z. Xing, G. Xu, J. Han, G. Chen, B. Lu, S. Liang, J. Zhou, *Trends Chem.* **2023**, 5(5), 380–392.
- [7] Y. Niu, D. Wang, Y. Ma, L. Zhi, *Chin. Chem. Lett.* **2022**, 33(3), 1430–1434.
- [8] Y. Dai, C. Zhang, J. Li, X. Gao, P. Hu, C. Ye, H. He, J. Zhu, W. Zhang, R. Chen, *Adv. Mater.* **2024**, 36(14), 2310645.
- [9] V. Augustyn, P. Simon, B. Dunn, *Energy Environ. Sci.* **2014**, 7(5), 1597–1614.
- [10] Y. Qin, X. Wang, *Angew. Chem. Int. Ed.* **2024**, 63(2), e202315464.
- [11] D. W. Smith, *J. Chem. Educ.* **1977**, 54(9), 540.
- [12] X. Dou, X. Xie, S. Liang, G. Fang, *Sci. Bull.* **2024**, 69(6), 833–845.
- [13] Y. Kim, Y. Park, M. Kim, J. Lee, K. J. Kim, J. W. Choi, *Nat. Commun.* **2022**, 13(1), 2371.
- [14] Y. Lu, T. Zhu, W. van den Bergh, M. Stefik, K. Huang, *Angew. Chem. Int. Ed.* **2020**, 132(39), 17152–17159.
- [15] W. Zhou, H. J. Fan, D. Zhao, D. Chao, *Natl. Sci. Rev.* **2023**, 10(12), nwad265.
- [16] S. Tian, T. Hwang, S. Malakpour Estalaki, Y. Tian, L. Zhou, T. Milazzo, S. Moon, S. Wu, R. Jian, K. Balkus Jr, *Adv. Energy Mater.* **2023**, 2300782.
- [17] D. G. Vazquez, T. P. Pollard, J. Mars, J. M. Yoo, H.-G. Steinrück, S. E. Bone, O. V. Safonova, M. F. Toney, O. Borodin, M. R. Lukatskaya, *Energy Environ. Sci.* **2023**, 16(5), 1982–1991.
- [18] Y. Zhong, X. Xie, Z. Zeng, B. Lu, G. Chen, J. Zhou, *Angew. Chem. Int. Ed.* **2023**, 62(40), e202310577.
- [19] X. Xie, H. Fu, Y. Fang, B. Lu, J. Zhou, S. Liang, *Adv. Energy Mater.* **2022**, 12(5), 2102393.
- [20] G. Li, Z. Zhao, S. Zhang, L. Sun, M. Li, J. A. Yuwono, J. Mao, J. Hao, J. Vongsvivut, L. Xing, *Nat. Commun.* **2023**, 14(1), 6526.
- [21] C. Wang, X. Zeng, J. Qu, J. M. Cairney, Q. Meng, P. J. Cullen, Z. Pei, *Matter* **2023**, 6(11), 3993–4012.
- [22] B. Zhang, L. Qin, Y. Fang, Y. Chai, X. Xie, B. Lu, S. Liang, J. Zhou, *Sci. Bull.* **2022**, 67(9), 955–962.
- [23] X. Tang, P. Wang, M. Bai, Z. Wang, H. Wang, M. Zhang, Y. Ma, *Adv. Sci.* **2021**, 8(23), 2102053.
- [24] Z. Khan, D. Kumar, X. Crispin, *Adv. Mater.* **2023**, 35(36), 2300369.

- [25] J. Han, A. Mariani, S. Passerini, A. Varzi, *Energy Environ. Sci.* **2023**, 16(4), 1480–1501.
- [26] W. Wang, C. Li, S. Liu, J. Zhang, D. Zhang, J. Du, Q. Zhang, Y. Yao, *Adv. Energy Mater.* **2023**, 13(18), 2300250.
- [27] Y. Lv, Y. Xiao, L. Ma, C. Zhi, S. Chen, *Adv. Mater.* **2022**, 34(4), 2106409.
- [28] Z. Lv, Y. Kang, G. Chen, J. Yang, M. Chen, P. Lin, Q. Wu, M. Zhang, J. Zhao, Y. Yang, *Adv. Funct. Mater.* **2024**, 34(3), 2310476.
- [29] W. B. Tu, S. Liang, L. N. Song, X. X. Wang, G. J. Ji, J. J. Xu, *Adv. Funct. Mater.* **2024**, 2316137.
- [30] Z. Zhao, B. Nian, Y. Lei, Y. Wang, L. Shi, J. Yin, O. F. Mohammed, H. N. Alshareef, *Adv. Energy Mater.* **2023**, 13(21), 2300063.
- [31] Y. Xiang, H. Pan, Y. Jiang, S. Xie, M. Xu, X. Zhang, *Nano Energy* **2023**, 117, 108873.
- [32] H. Yang, C.-A. Wang, Y. Dong, *Adv. Powder Mater.* **2024**, 100185.
- [33] S. Guo, L. Qin, C. Hu, L. Li, Z. Luo, G. Fang, S. Liang, *Adv. Energy Mater.* **2022**, 12(25), 2200730.
- [34] H. Yang, Z. Chang, Y. Qiao, H. Deng, X. Mu, P. He, H. Zhou, *Angew. Chem. Int. Ed.* **2020**, 132(24), 9463–9467.
- [35] F. Zhao, J. Feng, H. Dong, R. Chen, T. Munshi, I. Scowen, S. Guan, Y. E. Miao, T. Liu, I. P. Parkin, *Adv. Funct. Mater.* **2024**, 2409400.
- [36] H. Ge, L. Qin, B. Zhang, L. Jiang, Y. Tang, B. Lu, S. Tian, J. Zhou, *Nanoscale Horiz.* **2024**. DOI: 10.1039/D4NH00243A.
- [37] W. Nie, F. Tian, L. Zhang, L. Chang, Q. Sun, T. Duan, X. Lu, H. Cheng, *Adv. Funct. Mater.* **2024**, 2403305.
- [38] Z. Liu, X. Luo, L. Qin, G. Fang, S. Liang, *Adv. Powder Mater.* **2022**, 1(2), 100011.
- [39] C. Xia, J. Guo, Y. Lei, H. Liang, C. Zhao, H. N. Alshareef, *Adv. Mater.* **2018**, 30(5), 1705580.
- [40] Y. Liu, X. Wu, *Nano Energy* **2021**, 86, 106124.
- [41] M. S. Chae, D. Setiawan, H. J. Kim, S.-T. Hong, *Batteries* **2021**, 7(3), 54.
- [42] P. He, G. Zhang, X. Liao, M. Yan, X. Xu, Q. An, J. Liu, L. Mai, *Adv. Energy Mater.* **2018**, 8(10), 1702463.
- [43] G. Yang, Q. Li, K. Ma, C. Hong, C. Wang, *J. Mater. Chem. A* **2020**, 8(16), 8084–8095.
- [44] Y. Ran, J. Ren, Y. Kong, B. Wang, X. Xiao, Y. Wang, *Electrochim. Acta* **2022**, 412, 140120.
- [45] R. Chen, C. Zhang, J. Li, Z. Du, F. Guo, W. Zhang, Y. Dai, W. Zong, X. Gao, J. Zhu, *Energy Environ. Sci.* **2023**, 16(6), 2540–2549.
- [46] C. Li, W. Wu, Y. Liu, X. Yang, Z. Qin, Z. Jia, X. Sun, *J. Power Sources* **2022**, 520, 230853.
- [47] B. Lan, Z. Peng, L. Chen, C. Tang, S. Dong, C. Chen, M. Zhou, C. Chen, Q. An, P. Luo, *J. Alloys Compd.* **2019**, 787, 9–16.
- [48] F. Wan, L. Zhang, X. Dai, X. Wang, Z. Niu, J. Chen, *Nat. Commun.* **2018**, 9(1), 1656.
- [49] X. Wang, B. Xi, X. Ma, Z. Feng, Y. Jia, J. Feng, Y. Qian, S. Xiong, *Nano Lett.* **2020**, 20(4), 2899–2906.
- [50] Q. Li, X. Ye, H. Yu, C. Du, W. Sun, W. Liu, H. Pan, X. Rui, *Chin. Chem. Lett.* **2022**, 33(5), 2663–2668.
- [51] H. Luo, B. Wang, C. Wang, F. Wu, F. Jin, B. Cong, Y. Ning, Y. Zhou, D. Wang, H. Liu, *Energy Storage Mater.* **2020**, 33, 390–398.
- [52] H. Luo, B. Wang, F. Wang, J. Yang, F. Wu, Y. Ning, Y. Zhou, D. Wang, H. Liu, S. Dou, *ACS Nano* **2020**, 14(6), 7328–7337.
- [53] Y. Zhao, S. Liang, X. Shi, Y. Yang, Y. Tang, B. Lu, J. Zhou, *Adv. Funct. Mater.* **2022**, 32(32), 2203819.
- [54] W. Yang, W. Yang, Y. Huang, C. Xu, L. Dong, X. Peng, *Chin. Chem. Lett.* **2022**, 33(10), 4628–4634.
- [55] H. Shen, S. Jing, S. Liu, Y. Huang, F. He, Y. Liu, Z. Zhuang, Z. Zhang, F. Liu, *Adv. Powder Mater.* **2023**, 2(4), 100136.
- [56] X. Liu, W. Kang, X. Li, L. Zeng, Y. Li, Q. Wang, C. Zhang, *Nano Mater. Sci.* **2023**, 5(2), 210–227.
- [57] Y. Pan, Z. Liu, S. Liu, L. Qin, Y. Yang, M. Zhou, Y. Sun, X. Cao, S. Liang, G. Fang, *Adv. Energy Mater.* **2023**, 13(11), 2203766.
- [58] J. Li, Z. Liu, S. Han, P. Zhou, B. Lu, J. Zhou, Z. Zeng, Z. Chen, J. Zhou, *Nano-Micro Lett.* **2023**, 15(1), 237.
- [59] F. Li, C. Zhou, J. Zhang, Y. Gao, Q. Nan, J. Luo, Z. Xu, Z. Zhao, P. Rao, J. Li, *Adv. Mater.* **2024**, 2408213.

Manuscript received: June 26, 2024

Accepted manuscript online: August 28, 2024

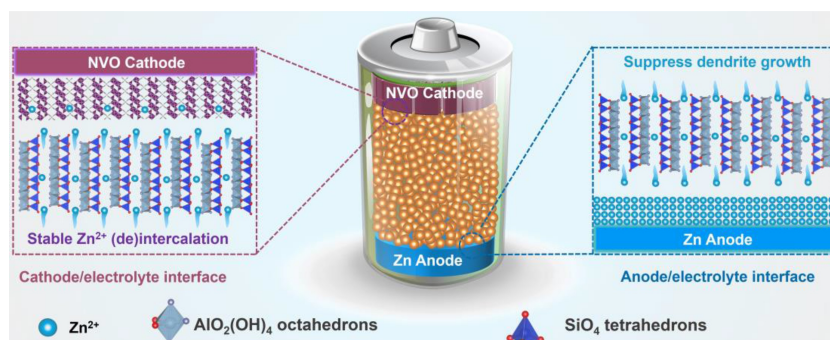
Version of record online: ■■■, ■■■

Research Article

Zinc Metal Batteries

C. Zhou, Z. Wang, Q. Nan, H. Wen, Z. Xu,
J. Zhang, Z. Zhao, J. Li, Z. Xing, P. Rao,
Z. Kang, X. Shi,* X. Tian* — e202412006

Simultaneous Inhibition of Vanadium Dissolution and Zinc Dendrites by Mineral-Derived Solid-State Electrolyte for High-Performance Zinc Metal Batteries



Kaolin is demonstrated as an effective material to prepare Zn-based solid electrolyte (KL-Zn), which simultaneously eliminates the interfacial side reactions of zinc anode and inhibits the vanadium

dissolution of $\text{NH}_4\text{V}_4\text{O}_{10}$ cathode, endowing high reversible capacity and superior cyclic stability for Zn// $\text{NH}_4\text{V}_4\text{O}_{10}$ batteries.